



# Catalytic current mapping of oxygen reduction on isolated Pt particles by atomic force microscopy-scanning electrochemical microscopy

Srikanth Kolagatla, Palaniappan Subramanian, Alex Schechter\*

Department of Chemical Sciences, Ariel University, Ariel 40700, Israel

## ARTICLE INFO

### Keywords:

Electrochemical current mapping  
Oxygen reduction reaction  
Pt nanoparticles  
Catalytic mapping  
AFM-SECM

## ABSTRACT

A fundamental understanding of active oxygen reduction sites on individual Pt nanoparticles is essential for the efficient utilization of Pt particles in electrocatalytic reactions. Here we use a modified Atomic Force Microscopy-Scanning Electrochemical Microscopy (AFM-SECM) to measure catalytic current responses of individual Pt particles on a nanometric scale. The ORR activity of an individual unsupported Pt nanoparticle and carbon-supported Pt aggregates at different ORR reduction potentials were mapped using a 50 nm diameter Pt wire electrode embedded in a SiO<sub>2</sub> tip, positioned at a ~4 nm working distance above the surface. In this work, both the oxygen reduction and peroxide generation active sites were identified by performing electrochemical current mapping on the same Pt nanoparticle. The implications as well as the limitation of this new catalytic study approach is discussed based on the model of O<sub>2</sub> reduction.

## 1. Introduction

The oxygen reduction reaction (ORR) is one of the most important reactions in electrochemistry, and yet its slow kinetics hinders the improvement of low-temperature fuel cell performance [1]. Enhancing the electro catalytic activity of Pt-based catalysts and consequently reducing the Pt loading without compromising the activity is imperative to the commercialization of fuel cells, particularly for automotive applications [2].

The ORR in acidic media involves four electrons to produce H<sub>2</sub>O (Eq. (1)), but hydrogen peroxide (H<sub>2</sub>O<sub>2</sub>) is the intermediate byproduct when the ORR proceeds through a two-electron reaction (Eq. (2)).



Significant efforts have been dedicated experimentally and computationally to improve our understanding of the shape, size and structure-activity relationship of the ORR on a Pt [3–5] catalyst. Most experimental studies relating to highly dispersed Pt nanoparticles (Pt-NPs) are limited to distribution of Pt-NP sizes synthesized on high-surface-area carbons. These studies indicate either that the surface activity is independent of size [6], or more often the activity of 1, 3 and 5 nm Pt-NPs remains constant [7]. The catalytically active centers in highly dispersed Pt-NPs and nanoaggregates (NAs) on carbon electrodes still remain ambiguous [7,8]. As a result, no conclusive strategy has

been devised so far for designing Pt-NPs with optimal ORR activity, or for improving the utilization of state-of-the-art Pt catalysts in fuel cell electrodes. Electrochemical microscopic techniques that show the specific activity of highly dispersed Pt-NPs or aggregates are very scarce in the literature and typically display low lateral resolutions [9]. Further studies using these techniques have the potential to bring new insight into the most active and inactive ORR catalytic sites in a Pt particle [10].

Scanning electrochemical microscopy (SECM) [11] is a probe technique used for simultaneously obtaining the chemical properties, topography and catalytic property of the nanoparticle surfaces [12]. The substrate generation/tip collection (SG/TC) [13] mode of SECM has been successfully used for rapid screening of different combinations of bimetallic and ternary electrocatalysts [14,15]. SECM has also been used for imaging the electro catalytic activity of different platinum and gold nanoparticles that catalyze the ORR in acidic and basic media, respectively [16–21]. More recently, scanning electrochemical microscopy-scanning ion conductance microscopy (SECM-SICM) was used in combination to map the electrochemical hydrogen-peroxide generation process occurring on individual gold nanoparticles. The authors reported current mapping in the pA range over particles of ~500 nm with a ~1 μm electrode [22–25]. Unwin et al. reported mapping of electro catalysis at the zepto-molar (10<sup>−21</sup> M) level on single Pt nanoparticles over a carbon nanotube using the scanning electrochemical cell microscopy (SECCM) technique. The major disadvantages using the

\* Corresponding author.

E-mail address: [salex@ariel.ac.il](mailto:salex@ariel.ac.il) (A. Schechter).

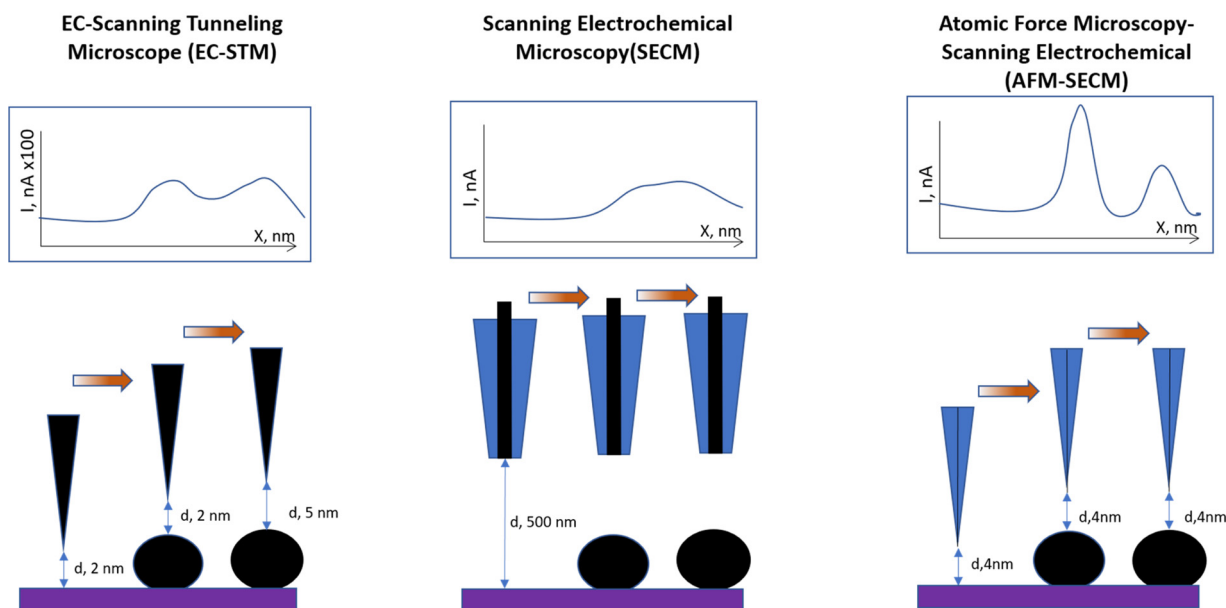
<https://doi.org/10.1016/j.apcatb.2019.117843>

Received 1 November 2018; Received in revised form 3 June 2019; Accepted 7 June 2019

Available online 15 June 2019

0926-3373/© 2019 Elsevier B.V. All rights reserved.

# Electrochemical Topography Methods



**Scheme 1.** Comparison of current measurement capabilities of prominent scanning electrochemical techniques.

above-said techniques are the large working distance and the tip size; the minimum separation distance achieved to date is 90 nm [16], which is very large when comparing the diffusion coefficient of the intermediates generated during the reaction. As a result, most of the intermediates generated during the reaction are diffused into the liquid before reaching the tip. In yet another report by Unwin et. al, a dual-barreled tip of 1  $\mu\text{m}$  in diameter positioned at a fixed height was employed to measure the electro catalytic currents. However, these measurements provided only an average catalytic current from the particle [26].

A comparison of prominent scanning electrochemical techniques used for simultaneously measuring topography and current is presented in Scheme 1 and Table 1. The electrochemical currents measured on a conducting particle surface are displayed as plots above each topography technique shown in the Scheme. Although scanning tunneling microscopy allows for topographical imaging with high spatial resolution, it superimposes the tunneling and reaction currents, which limits catalytic mapping resolution. The distance above the particle cannot be fixed as a constant when an electrochemical reaction is involved, and the total current ( $I_{\text{tot}} = I_{\text{tunneling}} + I_{\text{reaction}}$ ) is varied by the tunneling current and the reaction current. At the same time, electrochemical current mapping with higher sensitivity to surface topography can be measured using the AFM-SECM technique [27–30], which unlike traditional SECM does not require a current feedback loop to maintain a

fixed distance from the analyzed particle; it can map the catalytic current yielded exclusively from the reaction. Sensitivity to surface topography at high resolution is critical for mapping catalytic currents, since it may allow identification of defects/hotspots/active sites. This assumes greater significance when the catalytic surfaces are heterogeneous. Hence, this technique is ideally suited to discriminate between sites with different degrees of catalytic property.

In this work, AFM-SECM was used as an imaging tool, optimized to carry out measurements within a working distance of a few nanometers (4–8 nm) above the particle surface. We used a Pt embedded glass tip (herein referred as Pt tip) to scan the surface. It is important to note that the separation distance (distance between protruding end of Pt and working substrate) of 4 nm is smaller than the diffusion layer thickness of the electrode-electrolyte interface. Thus, the intermediate peroxide generated was collected under the tip, providing higher collection efficiency, electrochemical current mapping resolution of up to 16 nm, and topographic spatial resolution of 50 nm. The ORR active sites on Pt-NPs were identified by performing electrochemical current mapping using the Pt tip as the counter electrode, which helped confine the ORR right under the tip for monitoring of the working electrode current. Simultaneously, peroxide generation on the same particle was monitored by treating the Pt tip as a secondary working electrode under a constant peroxide oxidation potential. It was a very useful approach, enabling us to study the relationships of structure, electro catalytic

**Table 1**  
Features of different scanning probe methods used for catalytic current mapping.

Parameter/method	STM	SECCM/SICM	SECM	AFM-SECM
Separation distance	2 nm	> 500 nm	> 100 nm	4–8 nm
Positioning control	Bias current	Ion current	Redox current	Force modulation
Current range	nA	pA–nA	pA–nA	nA
Topography dependent current	Yes (Faradaic and tunneling current)	yes	yes	pure catalytic (constant distance)
Continuous scanning	yes	only in x direction (segmented images)	yes	yes
By-product ( $\text{H}_2\text{O}_2$ incase of ORR) detection	no	yes	yes	yes
Simultaneous measurement of topography and reaction independently	no	no	no	yes

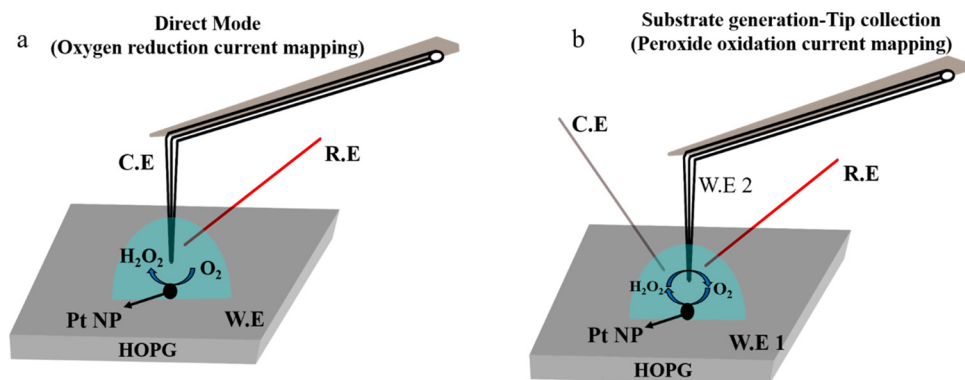


**Fig. 1.** Schematics of electrochemical setup used for performing (a) Oxygen reduction current mapping (b) Intermediate peroxide oxidation current mapping. W.E: working electrode, C.E: counter electrode, R.E: Quasi reference electrode. (Blue hemispherical shape represents the 2d-view of the liquid droplet). (For interpretation of the references to colour in this figure legend, the reader is referred to the web version of this article.)

activity and reaction byproducts of an individual Pt aggregate and its sub-particles, with higher collection efficiency and unprecedented spatial catalytic current mapping resolution.

## 2. Experimental

### 2.1. Materials and instruments

Commercial platinum black (Johnson Matthey), Nafion® suspension (5 wt% in isopropanol), acetonitrile (Acros Organics), perchloric acid (Merck), and acetone (Merck) were used as received. All the electrochemical measurements were carried out using a CHI 700E bipotentiostat (CH Instruments, US). Solutions were freshly prepared with ultrapure water (18 MΩ cm, Millipore Milli-Q). Highly oriented pyrolytic graphite (HOPG) was purchased from SPI Supplies (ZYG grade with a mosaic spread of  $0.8^\circ \pm 0.2^\circ$ ). The HOPG surface was freshly cleaved with adhesive tape, and then washed twice with acetone and distilled water to remove any traces of adhesive before performing each experiment. The AFM-SECM cell was made of Petri-dish shaped Teflon.

### 2.2. Preparation of Pt catalyst slurry

The Pt catalyst slurry was prepared by mixing commercial Pt powder, Nafion® suspension (5 wt%) and acetonitrile. The slurry was dispersed by ultra-sonication for 30 min. 2 μl of the catalyst ink was immediately dropped onto the HOPG surface to prepare it for AFM-SECM measurements.

### 2.3. Electrochemical setup and AFM-SECM current mapping experiments

AFM-SECM measurements were performed using a Nanonics Multiview 2000 AFM equipped with an AFM probe specially fabricated for electrochemical measurements. The AFM probe tip is made of a Pt wire laser-pulled through a glass pipette (Fig. S1). The protruding Pt tip is conductive and the cyclic voltammetric characterization of the tip performed in 0.1 M HClO<sub>4</sub> electrolyte is provided in Supporting information (Fig. S2). The tip curvature radius is 500 nm and the size of the protruding end of the Pt tip is 50 nm and the protrusion length is 200 nm. The lock-in frequency of the tip (resonance frequency of the AFM-SECM probe) is 38.72 kHz and the active quality factor (Q factor) is 1500. The value of Q factor was chosen to be higher because lower values in a liquid implies high forces between the tip and the sample in liquid of several nanonewtons that can produce a high deformation and damage in sample. These tips were supplied by Nanonics Supertips, Ltd. A computer-controlled bipotentiostat was used. Linear sweep voltammetry (LSV) and chronoamperometry (CA) measurements were performed using the built-in software. The positioning of the tip using a piezo actuator was done via the AFM system, and the electrochemical measurements were carried out independently. The piezo movement was synchronized with the tip current by reading the analog output

signal from the bipotentiostat, via a data acquisition board supplied with the AFM setup. All the metal parts in the room and the electronic equipment were grounded to prevent damage to the tip. To suppress thermal drift, all the measurements were performed in a Faraday cage and the whole setup was placed on a vibration-absorbing table.

### 2.4. AFM-SECM procedures and measurements

The glass-embedded Pt tip was positioned 4–8 nm above the HOPG substrate using a system-generated feedback approach, which replaced the existing approach curve method used in SECM technique for positioning the Pt tip close to the surface. AFM-SECM imaging was performed on Pt nanoaggregates (Pt-NAs) modified HOPG. The AFM-SECM tip typically scanned over a  $2 \mu\text{m} \times 2 \mu\text{m}$  area of the HOPG with a pixel density of  $256 \times 256$  pixels per image at a speed of 15 ms/point, scanning 25 lines per  $0.1 \mu\text{m}$  and recording a data point every 4 ms. The electrochemical measurements were performed using the “repetitive run” function available in CHI software. The currents at the substrate and at the tip were recorded simultaneously with the x, y and z position of the tip. Data acquisition was done with NSW AFM software. The active-sites distribution was obtained by accumulation of the active pixels at the selected current range, dividing that number by the total number of pixels (8060).

The oxygen reduction current mapping was performed using a three-electrode configuration (Fig. 1b), where the Pt embedded glass tip was used as a counter electrode in “direct mode” [11,31–33]. The oxygen reduction current mapping was done by monitoring the substrate currents confined right under the tip. The substrate generation/tip collection mode (SG/TC) method was used to measure the intermediate peroxide generated during the ORR reaction. A four-electrode electrochemical configuration (Fig. 1c) was used for SG/TC experiments, where the HOPG served as a primary working electrode (W.E. 1), the Pt tip as a secondary working electrode (W.E. 2), Pt wire as a counter electrode and a silver wire as a quasi-reference electrode. In this mode, the oxygen is reduced at the substrate and the formed peroxide intermediate diffuses towards the Pt tip (the amperometric sensor) located just 4–8 nm above the Pt NAs. It is then oxidized at the tip, which is polarized to 1.18 V vs. SHE, while the working electrode is polarized to 0.73 V vs. SHE. It is very important to note that ORR experiments and intermediate detection mapping experiments were done by modifying the electrode configurations without changing the measurement location of the primary working substrate (Pt-NAs modified HOPG). It is emphasized here that relatively higher currents are observed in peroxide oxidation current compared to oxygen reduction current due to the Pt wire used as a counter electrode, which has an area 10 orders of magnitude larger than the Pt tip. All experiments were carried out in an isothermal chamber at a relative humidity of over 40% maintained at 22 °C. All mapping experiments reported here are repeated at least 4 times to ensure reproducible results. Thus, the image contrast presented in the mapping images is well reproducible.

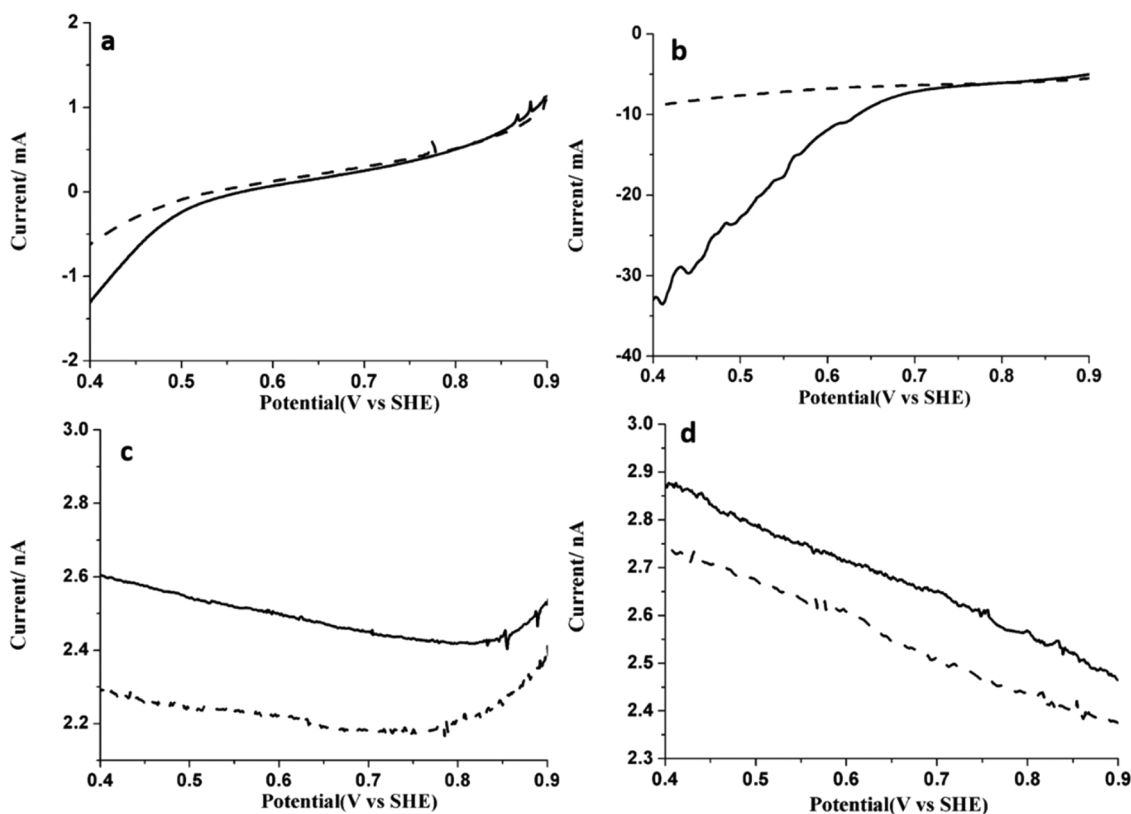


**Fig. 2.** Overlay of linear scan voltammogram in  $N_2$  saturated (dash line) and  $O_2$  saturated (solid line) 0.1 M  $HClO_4$  at a scan rate of 2 mV/s; (a) Bare HOPG surface, (b) Pt particle modified HOPG. Secondary working electrode (tip currents) of (c) Bare HOPG surface, (d) Pt particle modified HOPG surface.

The data presentation of ORR and peroxide oxidation current mapping is done side by side to show the experiments are done on the same selected area. The measured current cannot be directly compared since ORR and peroxide oxidation current mapping are two separate experiments done sequentially and not simultaneously.

### 3. Results and discussion

#### 3.1. Static mode electrochemical characterization

Electrochemical measurements were performed on the drop-coated Pt-NAs on the HOPG substrate in solutions of 0.1 M  $HClO_4$  under a  $N_2$  or  $O_2$  atmosphere at a potential scan rate of 2 mV/s. Fig. 2a,b displays the LSV measurements of the bare HOPG surface and Pt-NAs on HOPG in 0.1 M  $HClO_4$  under a  $N_2$  (dash line) and an  $O_2$  atmosphere (solid line). It should be noted that in this experiment, the AFM tip electrode was in static mode. The onset of the oxygen reduction process (a potential at which 1% of the maximal current is attained) was observed under  $O_2$  at 0.60 V and 0.73 V on bare HOPG and Pt-NAs, respectively. The background currents under  $N_2$  were clearly lower than in a  $O_2$ -saturated solution, providing clear evidence of catalytic activity of the Pt-NAs on the HOPG substrate. Part of the ORR current was emanating from the edges of the HOPG substrate, as demonstrated in our previous study [34] and in Fig. 2a.

Fig. 2c,d shows the peroxide oxidation currents on the tip, used here as a secondary working electrode to probe the peroxide formation by measuring the oxidation currents of  $H_2O_2$  released over the catalyst during the LSV experiment (Fig. 2a,b). The experiments were conducted in a  $N_2$  atmosphere (dash line) and an  $O_2$  atmosphere (solid line) while holding the tip electrode potential at 1.18 V (vs. SHE). This potential is below water oxidation and above oxygen reduction potentials. On the bare HOPG surface, an increase of 0.3 nA current was observed when comparing the  $N_2$  and  $O_2$  voltammograms. However, above the Pt

aggregate, the detected  $H_2O_2$  oxidation currents were significantly smaller, with only an increase of 0.15 nA above the background; this is in line with high  $H_2O_2$  formation above graphitic/carbonaceous ORR catalysts. This small  $H_2O_2$  current, obtained by placing the tip at a nanometric separation distance (4–8 nm) and using a force feedback control loop, was compared to the total  $O_2$  currents observed in LSV experiments. Our finding reflected the low local formation of this by-product above a random Pt particle. We also observed some ORR catalytic activity exhibited by the HOPG through formation of  $H_2O_2$ ; hence, the oxidation of peroxide species was assumed to have contributed to the oxidative current measured below 0.73 V [24,35,36]. It should be emphasized here that the measurements presented above corresponded to the activity of Pt-NAs over the *entire* electrode surface; these relatively large currents were not specific to any individual Pt-NAs. In another stage, we studied the activity of individual Pt-NAs of different sizes, using oxygen reduction and peroxide oxidation current mapping experiments.

#### 3.2. Electro catalytic current mapping

##### 3.2.1. ORR activity on a Pt aggregate

Fig. 3a displays the topography of the Pt-NAs on the HOPG surface. The Pt-NAs are 350 nm in diameter and 20 nm in height (Fig. 3b) and are comprised of an ensemble of smaller particles measuring 50–80 nm. Oxygen reduction current mapping of the Pt-NAs at a potential of 0.78 V (presented in Fig. 3c) indicated a high-resolution image of ORR reduction current with a peak current of 40 nA. The currents on Pt-NAs were relatively higher when compared with those measured on the HOPG surface or currents reported by others [16]. The currents generated in our experiments are higher than the reported values in the literature, but the experimental conditions are also different from other groups. For instance, the highest separation distance attained using SECM technique reported by Bard's group [37] is 10 nm and much



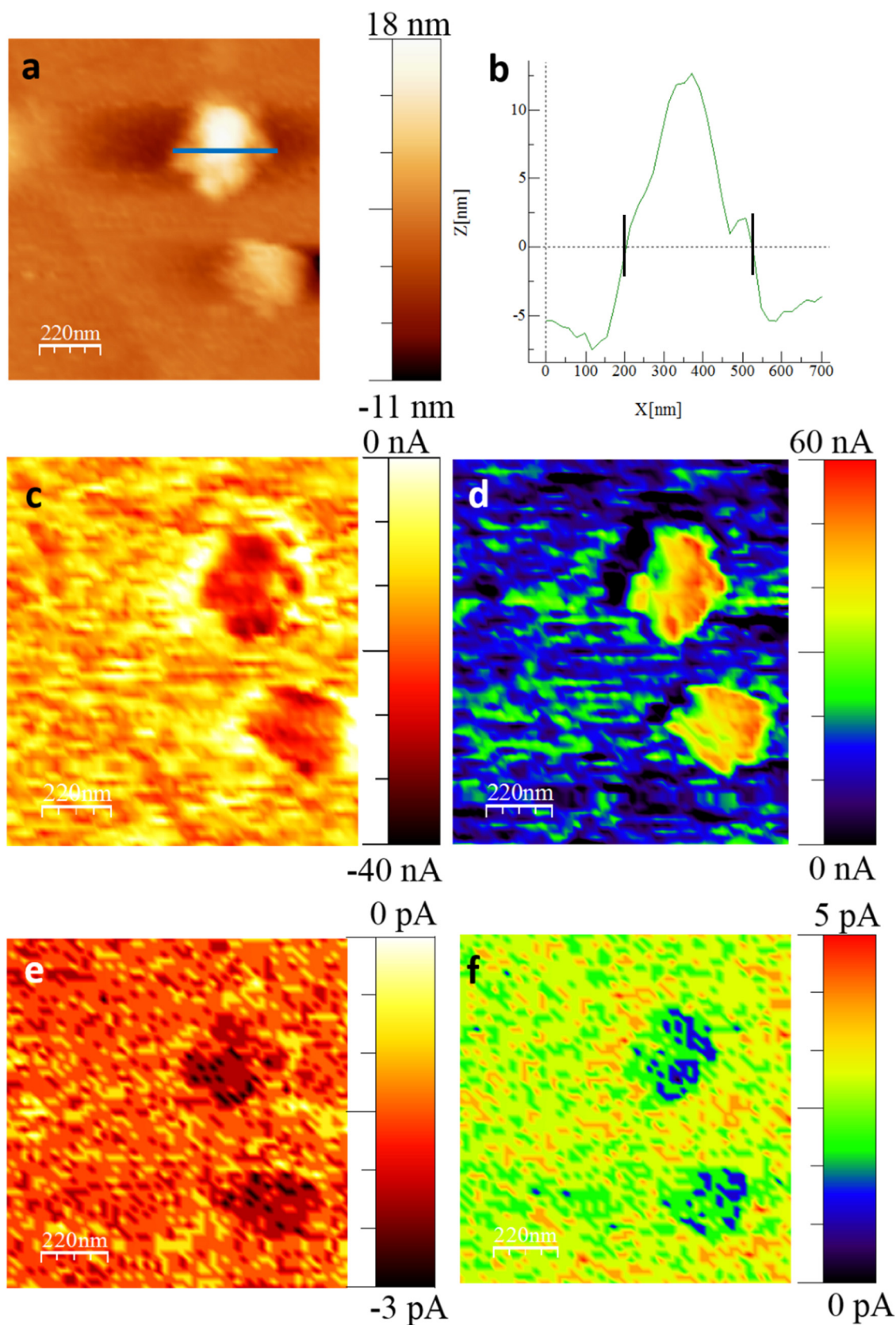


**Fig. 3.** (a) AFM-SECM height image of Pt-NAs on HOPG surface, (b) Z-axis height profile, oxygen reduction current mapping, and peroxide oxidation current mapping in (c, d) 0.1 M HClO<sub>4</sub> and (e, f) in 0.1 M HClO<sub>4</sub> + 10 ppm Na<sub>2</sub>S respectively. Potential applied to the substrate is 0.78 V vs SHE and the potential applied to the tips is 1.18 V vs SHE.

lower concentrations of 2 mM. In our case, the tip was positioned at a 4–8 nm separation distance which is within the diffusion layer thickness and results in higher  $O_2$  reduction and efficient collection of intermediates. In addition, the proximity of the Pt tip to the surface provides constant flow of  $O_2$  from water oxidation on the tip, which has an important influence on the concentration of the electrolyte confined in the very small volume between the substrate and tip. The calculated concentration of oxygen generated by 50 nA is 0.41 mol/L. Similarly, the peroxide oxidation current mapping (shown in Fig. 3d) displayed a very high oxidation current with a maximum of 60 nA. It should be recalled that in this experiment, the tip was used as a sensing electrode, while the counter electrode was a 0.3 mm diameter Pt wire hanging above the substrate (Fig. 1c). While using the larger surface area counter electrode in a 4-electrode-system, the whole surface of the substrate (working electrode) becomes active in ORR as well as in  $H_2O_2$  formation. The Pt tip placed at 4 nm above the surface merely measures the accumulated  $H_2O_2$  and therefore is expected to display higher currents. Moreover, the tip is also moving along the surface so there is no problem of concentration depletion. When ORR current mapping is done using a 3-electrode configuration with the 50 nm Pt tip serving as counter electrode, the total currents are 5 orders of magnitude lower (Fig. 2a,b) and accordingly the  $H_2O_2$  concentration is expected to be smaller. However, we could not measure the ORR and  $H_2O_2$  oxidation on the tip simultaneously. Therefore, the  $H_2O_2$  mapping provides a qualitative image of the areas on the single Pt particle active in  $H_2O_2$  formation and a comparison to ORR of the same scanned site but cannot be directly compared.

A comparison of the topographic image and the ORR current mapping clearly supports the understanding that the reaction occurred in designated sites throughout the agglomerate rather than on distinct points of a larger  $z$  value. Most of the higher current sites were in the peripheral regions of the Pt-NAs rather than in the center; we attributed this to a wider diffusion field into these areas.

The AFM-SECM characterization of drop-casted Pt-NAs was further studied by repeating the catalytic current mapping in a solution of 0.1 M  $HClO_4$  containing 10 ppm  $Na_2S$ .  $Na_2S$  is converted to  $H_2S$  under acidic conditions, which is known to poison Pt catalysts [38] and instantly inhibit the oxygen reduction process on Pt. Fig. 3e displays the ORR current mapping measurements performed in the  $Na_2S$  solution. The observed maximal current decreased by 4 orders of magnitude to 3 pA, indicating that the ORR activity of the Pt-NAs specifically ceased on the Pt surface at the formerly detected active spots. Further confirmation of the activity loss associated with the studied particle is inferred by the absence of peroxide oxidation currents (Fig. 3f). Significant loss of ORR currents measured during the poisoning experiments proved that the source of the oxygen reduction currents was indeed the Pt-NAs.

### 3.2.2. The effect of applied potential on the mapped currents

The AFM-SECM height images of an ensemble of three Pt-NAs (each one ~200 nm in width and 350–600 nm in length) are presented in Fig. 4a, assigned numbers “1”, “2” and “3”. Fig. 4c shows the oxygen reduction activity of the Pt-NAs at an applied potential of 0.73 V, close to the onset potential of the ORR reaction (Fig. 2b) and well within the kinetic potential range. Only aggregates “1” and “2” show oxygen reduction activity, with a maximum current of 30 and 20 nA, respectively; while Pt-NA “3” did not show any noticeable oxygen reduction activity at this potential. Fig. 4d represents the corresponding peroxide oxidation currents, clearly marking higher currents on Pt-NAs “1” and “2” (in the range of 35 nA) and very low currents (10 nA) on Pt-NA “3” a close match with the ORR maps. The peroxide generation image analysis appeared to indicate that the local accumulation of this partial reduction byproduct served as a more sensitive probe for ORR active sites, as was evident by the small particles of 50 nm diameter that started to appear in this image (Fig. 4d) in the vicinity of the three regions. Oxygen reduction and peroxide oxidation current distribution are shown in Fig. 4e,f. A total of 76% of the surface exhibited

electrochemical activity towards oxygen reduction and 75% of this area also showed peroxide oxidation.

We then applied a potential of 0.68 V to the working electrode; the acquired current mapping images are presented in Fig. 4g,h. The oxygen reduction current mapping showed a pronounced increase in activity within and around Pt-NAs “1” and “2” (50 and 40 nA, respectively). However, little or no oxygen reduction current was observed across Pt-NA “3”. Reciprocal behavior was observed in peroxide oxidation current mapping, where an increase in peroxide generation was noticed at the center (70 nA) and borders (50 nA) of the Pt-NAs. The distribution chart (Fig. 4i,j) shows that 79% of the Pt deposits exhibited activity towards oxygen reduction, and 76% showed peroxide oxidation; this clearly demonstrated that active site utilization depends on potential. Current mapping at a potential bias of 0.63 V is presented in Fig. 4k,l. The measured currents were close to the values recorded at an applied potential of 0.68 V. However, the scanned surface showed an increase in oxygen reduction current (seen as expansion of red color) to much larger areas in the measured zone, to the total maximum value (~30 nA). The highest currents were mostly obtained under aggregates “1” and “2” (50 nA); yet the other regions of the surface, including those of aggregate “3”, showed oxygen reduction activity currents of only 30 nA in surface utilization. The increase of oxygen reduction in the high-current region constituted 88% of the total number of measured pixels, and 87% of the corresponding peroxide oxidation (Fig. 4m,n). These results are attributed to a contribution from the underlying HOPG surface, which was previously shown to be catalytically more active in ORR under similar higher over potentials [27]. This observation, namely that the catalytic currents of the active Pt sites do not exceed 50 nA at higher over potential, clearly proves that the ORR current of the Pt sites is limited by the mass transport of oxygen.

Hydrogen peroxide oxidation current mapping was largely distributed across the ORR active Pt sites, except for the top portion of the particle (preceding particle “1” Pt-NAs), where the high  $O_2$  reduction activity did not correspond to high local yield or concentration. We attribute this behavior to a more efficient  $4e^- + 4H^+$  of  $O_2$  reduction to water at this site, instead of the  $2e^-/2H^+$ ; a result which emphasizes the variation among particles with respect to their reaction mechanism behavior. The remaining Pt-NAs “2” and “3” and the bare HOPG showed peroxide oxidation currents of 60 nA. The peroxide oxidation currents observed on the HOPG surface, due to the ORR activity exhibited at the applied potential (0.63 V), is shown in the LSV trace presented in Fig. 2. Table 2 provides a comparison between the ORR and peroxide oxidation currents of all three particles at different potentials.

### 3.2.3. Particle size effect

The AFM-SECM topography images of Pt-NAs of 350 nm in diameter and less than 10 nm in height are shown in Fig. 5a,b. Fig. 5c depicts oxygen reduction current mapping of the Pt nuclei, performed by placing the tip at a constant separation distance of ~4 nm. The highest currents were measured in the center of the particle (marked “2”), while little or no (0 nA) activity was seen at the edges (marked “1”, “3”). The peroxide oxidation current mapping image is shown in Fig. 5d. The highest oxygen reduction activity (70 nA) came from the Pt particle center (marked “2”), whereas marginally lower currents (20 nA) were observed around the particle. This observation is mostly due to the diffusion of the peroxide, since no applicable ORR current was observed over the particle sites. The oxygen reduction and peroxide oxidation active pixel distribution chart (Fig. 5e,f) shows symmetrical peak current distribution, corresponding to 80% utilization of the surface towards oxygen reduction ( $X_i \times 100$ ), with 83% active in peroxide oxidation. This increase is likely related to peroxide diffusion during mapping. However, when normalizing the ORR surface utilization fraction ( $X_i$ ) by the physical area fraction occupied by this 350 nm particle ( $X_s = 0.024$ ), the resulting active Pt surface utilization ( $X_i/X_s$ ) was 0.33, which means that two-thirds of the particle's area remained

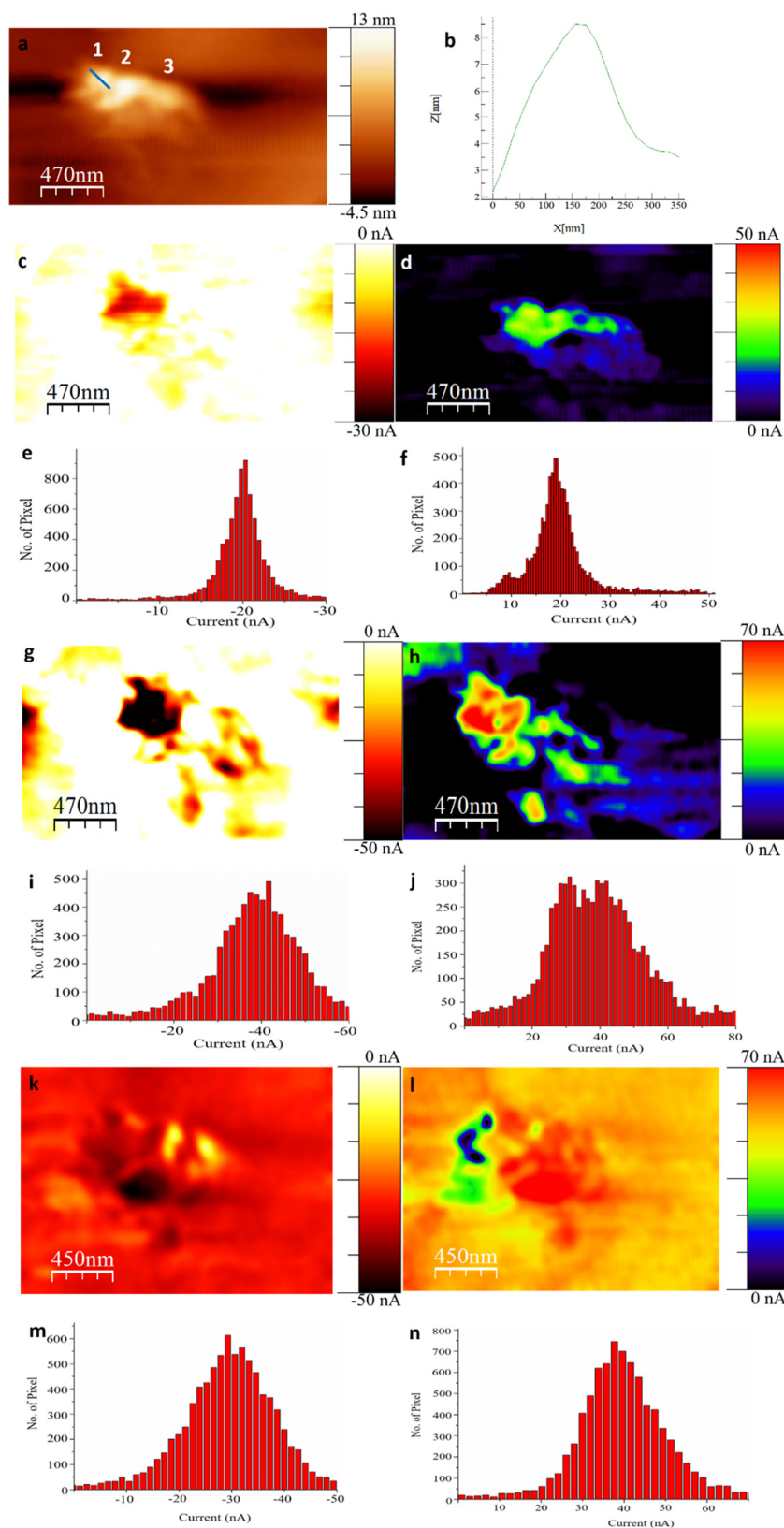


**Fig. 4.** (a) AFM-SECM height image of Pt-NPA on HOPG surface, (b) Z-axis height profile. Oxygen reduction current mapping and peroxide oxidation current mapping at 0.73 V (c, d); at 0.68 V (g, h), and at 0.63 V (k, l) respectively. Potential applied to the tips is 1.18 V vs SHE. Active pixel distribution of oxygen reduction and peroxide oxidation, respectively, at 0.73 V (e, f), at 0.68 V (i, j), and at 0.63 V (m, n). (For interpretation of the references to colour in the text, the reader is referred to the web version of this article.)



**Table 2**

ORR currents and peroxide oxidation currents on three different particles in the agglomerate (Fig. 4), measured at different potentials.

Potential	ORR current mapping			Peroxide oxidation currents		
	Pt-NA 1	Pt-NA 2	Pt-NA 3	Pt-NA 1	Pt-NA 2	Pt-NA 3
0.73 V	−30 nA	−20 nA	0 nA	35 nA	35 nA	20 nA
0.68 V	−50 nA	−40 nA	0 nA	70 nA	50 nA	40 nA
0.63 V	−40 nA	−20 nA	−20 nA	10 nA	70 nA	70 nA

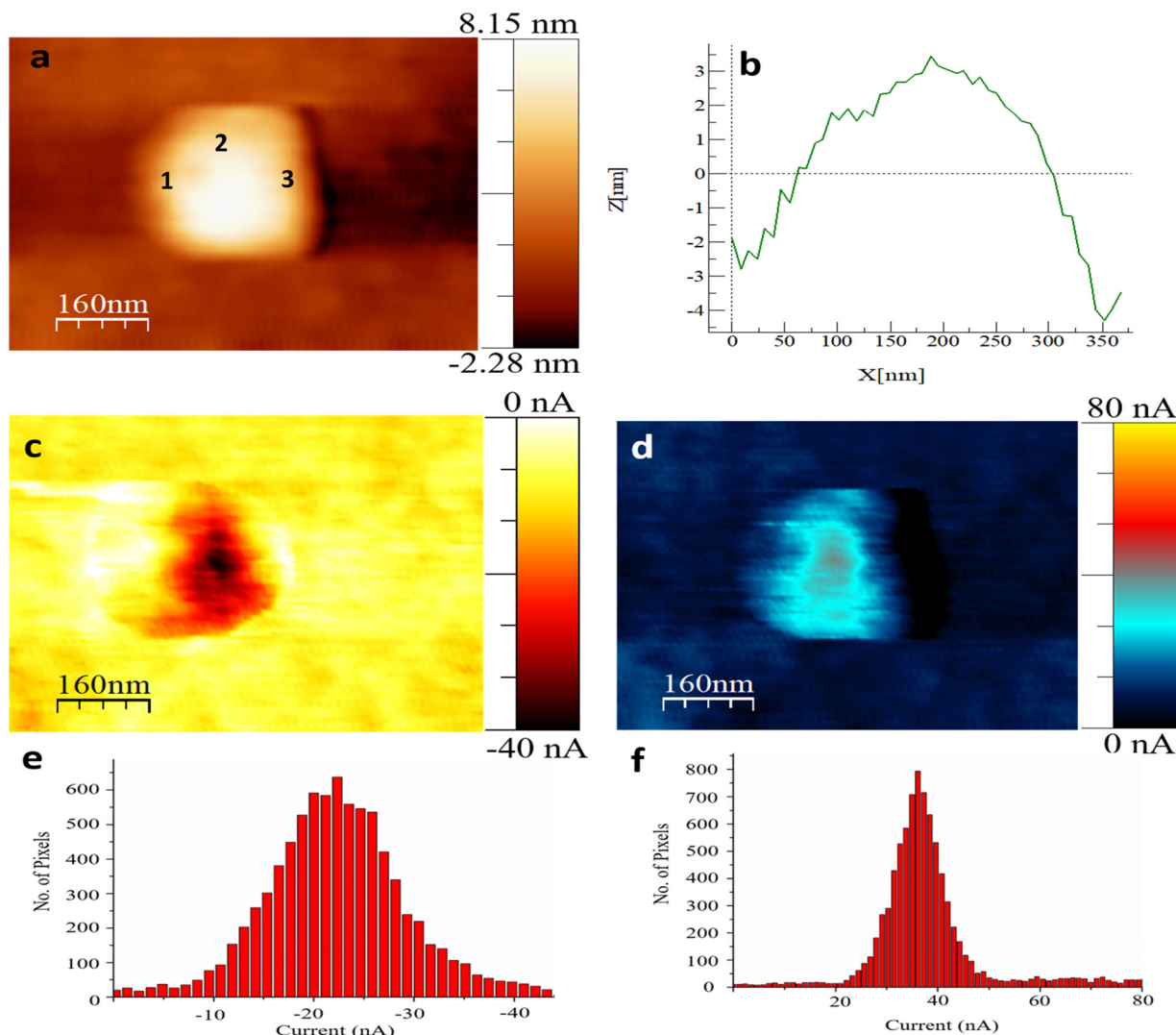
inactive.

Further, the effect of particle size on catalytic activity was studied using Pt-NAs of 800 nm in diameter and 120 nm in height (Fig. S3a–b). Fig. S3c–d displays the oxygen reduction and peroxide oxidation current mapping of the Pt-NAs, respectively. Oxygen reduction current mapping showed that the edges (marked “1”, “3”) of the Pt-NAs were the source of most of the activity (80 nA), while some areas in the Pt-NAs did not show oxygen reduction currents at all. The peroxide oxidation current mapping also mirrored the observation made in more catalytically active regions of Pt-NAs (edge sites: 160 nA). However, activity (100 nA) was also seen in the center of the Pt-NAs (shown in green color) where there were no measurable oxygen reduction

currents. This may suggest that some areas on the Pt-NAs were completely inactive toward oxygen reduction reaction. In the scanned 800 nm Pt-NAs, the percentage of active pixels (Fig. S3e, f) towards oxygen reduction and peroxide oxidation were 73% and 76%, respectively. The fraction of physical area occupied by this larger particle was  $X_s = 0.12$ ; hence, the total active Pt surface utilization was only 5.5% ( $X_i/X_s = 0.73/0.125$ ). In other words, the active Pt surface utilization on the larger, less uniform 800 nm particles was 5.8 times lower than on smaller, compact NPs. But more importantly, most of the Pt remained inactive on both particles.

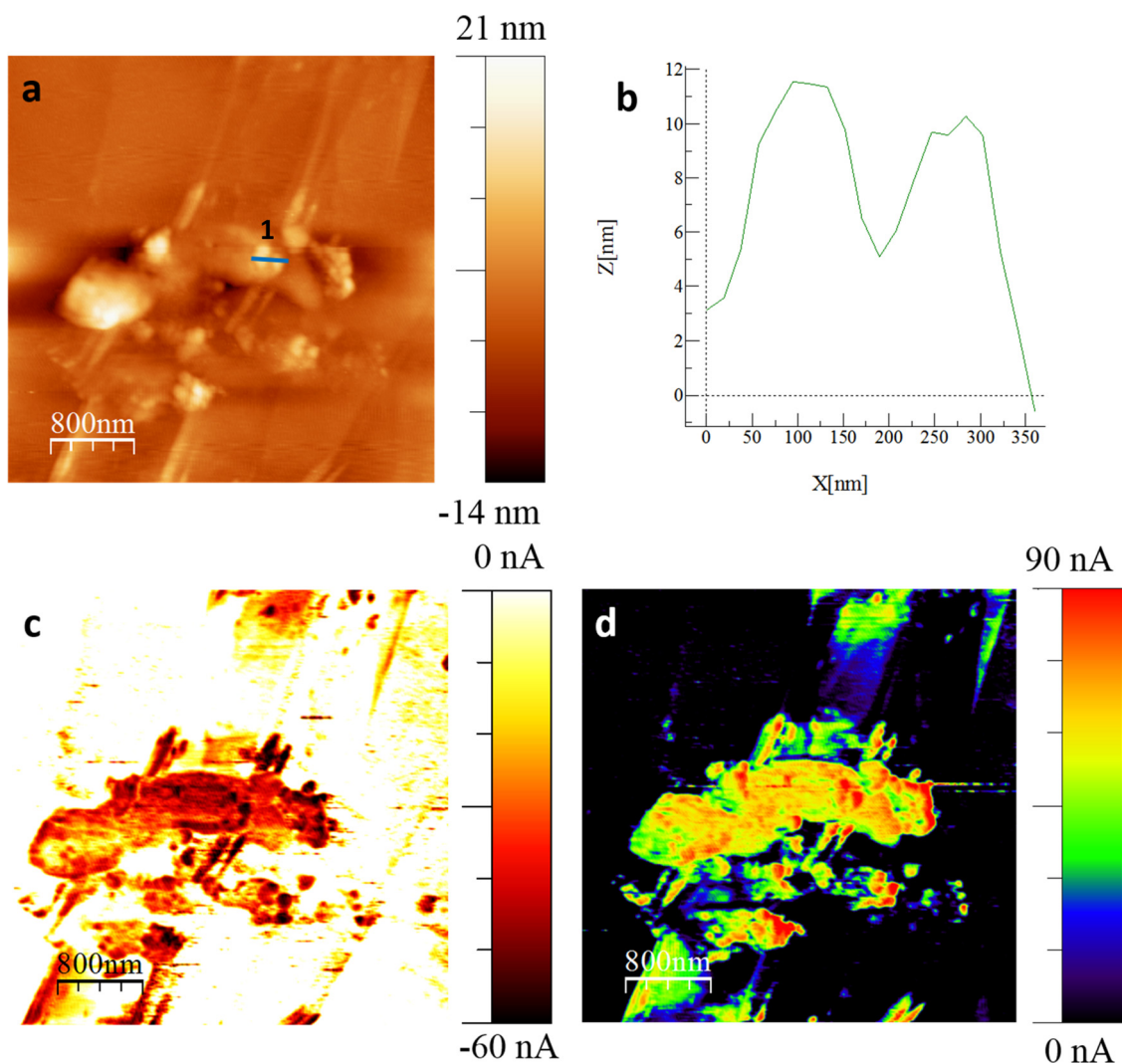
### 3.2.4. Mapping of carbon supported Pt-NPs

Fig. 6a displays a AFM-SECM topography image of Pt-NPs with a typical diameter of 100–300 nm and 20 nm in height on a disordered XC72 carbon support of 2.4  $\mu\text{m}$  in length. Some of the Pt-NPs were located above the carbon, and others were dispersed randomly on the support. An image of AFM-SECM current mapping presented in Fig. 6c exhibits ORR currents of 60 nA on the particles located on top of the carbon support (marked “1” in Fig. 6a). Pt-NPs separated from the carbon support had better accessibility to oxygen for catalytic reaction, which was similar to the value obtained (40 nA) from unsupported Pt on HOPG (seen as black in Fig. 5c). The Pt-NPs located on the inner parts of the carbon support showed a 10–15 nA decrease in currents



**Fig. 5.** (a–f) 350 nm Pt-NAs; (a) AFM-SECM height image, (b) Z-axis height profile, (c) Oxygen reduction current mapping potential applied to the substrate is 0.73 V vs SHE, (d) Peroxide oxidation current mapping potential applied to the tips is 1.18 V vs SHE, (e, f) Active pixel distribution of oxygen reduction and peroxide oxidation on HOPG, respectively.





**Fig. 6.** (a) AFM-SECM height image of Pt particle aggregate supported on carbon, (b) Z-axis height profile, (c) Oxygen reduction current mapping, potential applied to the substrate is 0.73 V vs SHE, (d) Peroxide oxidation current mapping, potential applied to the Pt tip is 1.18 V vs SHE.

(40–45 nA). However, these values were double compared to the bare carbon activity, which depicted maximal reduction currents of only 20 nA. Peroxide oxidation currents observed on the Pt-NPs was ~90 nA (Fig. 6d). The peroxide current mapping images displayed identical locations of oxygen reduction and peroxide oxidation currents, confirming that the Pt-NPs were active towards oxygen reduction reaction. Peroxide oxidation currents were measured without ORR in a few areas only. This may have been due to the diffusion of peroxide generated on the adjacent Pt-NPs.

Current mapping clearly showed the activity differences on Pt-NPs (60 nA), Pt-NP impregnated carbon (40 nA), bare XC72 carbon support (20 nA), and HOPG edges (2 nA). A clear trend was noticed from the measured catalytic currents on the different catalytic surfaces. Therefore, it is reasonable to argue that Pt-NP current distribution plays a major role in catalytic activity, and that there is a loss of activity when mixed with conductive support (although interestingly enough, bare XC72 carbon also showed slight activity towards ORR).

#### 4. Conclusions

An interesting approach based on AFM-SECM technique was explored in the study of active ORR catalytic sites involving individual Pt-NPs, which were either directly drop-casted or used as carbon-supported Pt-NPs on a HOPG surface. We managed to identify different

sites of ORR activity by using electrochemical current mapping at a spatial resolution of 16 nm. We applied a simultaneous force feedback loop to direct the ORR electrochemical reaction above single Pt-NPs and Pt-NAs, which functioned independently from the studied reaction. A supplementary SG-TC mode was used for probing the intermediate peroxide generated during the oxygen reduction reaction on the same Pt-NPs, via nanometer spatial resolution. Here we verified the catalytic activity of Pt-NPs by performing a poisoning experiment. Activity mapping of Pt-NPs of different sizes were studied, which showed varied catalytic activity sites. While larger particles exhibited higher ORR and complementary activity, particles of 300 nm or less produced the same currents. The distribution of the active sites was associated with accessibility of oxygen to the peripheries of the shape. However, certain areas (“hotspots”) in the centers of the particles produced high currents at lower relative potentials. On the other hand, other parts of the particles remained inactive even at high over potential, which could account for the low utilization of the Pt catalyst. The analytical approach presented in this work can be used for the general study of the effects of size and structure on catalytic activity in a variety of metallic NPs.

#### Acknowledgements

A.S. acknowledges the Israel Science Foundation (ISF) for funding the research work through the Israel National Research Center for

Electrochemical Propulsion (INREP) and I-CORE Program (number 2797/11). S.K and P.S. acknowledge the support of INREP and Ariel University for providing research scholarship.

## Appendix A. Supplementary data

Supplementary material related to this article can be found, in the online version, at doi:<https://doi.org/10.1016/j.apcatb.2019.117843>.

## References

- [1] H.A. Gasteiger, S.S. Kocha, B. Sompalli, F.T. Wagner, Activity benchmarks and requirements for Pt, Pt-alloy, and non-Pt oxygen reduction catalysts for PEMFCs, *Appl. Catal. B: Environ.* 56 (2005) 9–35, <https://doi.org/10.1016/j.apcatb.2004.06.021>.
- [2] R.R. Adzic, J. Zhang, K. Sasaki, M.B. Vukmirovic, M. Shao, J.X. Wang, A.U. Nilekar, M. Mavrikakis, J.A. Valerio, F. Uribe, Platinum monolayer fuel cell electrocatalysts, *Top. Catal.* 46 (2007) 249–262, <https://doi.org/10.1007/s11244-007-9003-x>.
- [3] K. Kinoshita, Particle size effects for oxygen reduction on highly dispersed platinum in acid electrolytes, *J. Electrochem. Soc.* 137 (1990) 845–848, <https://doi.org/10.1149/1.2086566>.
- [4] V. Komanicky, H. Lddir, K.C. Chang, A. Menzel, G. Karapetrov, D. Hennessy, P. Zapol, H. You, Shape-dependent activity of platinum array catalyst, *J. Am. Chem. Soc.* 131 (2009) 5732–5733, <https://doi.org/10.1021/ja900459w>.
- [5] B.R. Cuenya, Synthesis and catalytic properties of metal nanoparticles: size, shape, support, composition, and oxidation state effects, *Thin Solid Films* 518 (2010) 3127–3150, <https://doi.org/10.1016/j.tsf.2010.01.018>.
- [6] M. Watanabe, H. Sei, P. Stonehart, The influence of platinum crystallite size on the electroreduction of oxygen, *J. Electroanal. Chem. Interfac. Electrochem.* 261 (1989) 375–387, [https://doi.org/10.1016/0022-0728\(89\)85006-5](https://doi.org/10.1016/0022-0728(89)85006-5).
- [7] K.J.J. Mayrhofer, B.B. Bliznac, M. Arenz, V.R. Stamenkovic, P.N. Ross, N.M. Markovic, The impact of geometric and surface electronic properties of Pt-catalysts on the particle size effect in electrocatalysis, *J. Phys. Chem. B* 109 (2005) 14433–14440, <https://doi.org/10.1021/jp051735z>.
- [8] G.A. Tritsarlis, J. Greeley, J. Rossmeisl, J.K. Nørskov, Atomic-scale modeling of particle size effects for the oxygen reduction reaction on Pt, *Catal. Lett.* 141 (2011) 909–913, <https://doi.org/10.1007/s10562-011-0637-8>.
- [9] C.M. Sánchez-Sánchez, J. Solla-Gullón, F.J. Vidal-Iglesias, A. Aldaz, V. Montiel, E. Herrero, Imaging structure sensitive catalysis on different shape-controlled platinum nanoparticles, *J. Am. Chem. Soc.* 132 (2010) 5622–5624, <https://doi.org/10.1021/ja100922h>.
- [10] M. Nesselberger, S. Ashton, J.C. Meier, I. Katsounaros, K.J.J. Mayrhofer, M. Arenz, The particle size effect on the oxygen reduction reaction activity of Pt catalysts: influence of electrolyte and relation to single crystal models, *J. Am. Chem. Soc.* 133 (2011) 17428–17433, <https://doi.org/10.1021/ja207016u>.
- [11] D. Polcar, P. Dauphin-Ducharme, J. Mauzeroll, Scanning electrochemical microscopy: a comprehensive review of experimental parameters from 1989 to 2015, *Chem. Rev.* 116 (2016) 13234–13278, <https://doi.org/10.1021/acs.chemrev.6b00067>.
- [12] Y. Yu, T. Sun, M.V. Mirkin, Scanning electrochemical microscopy of single spherical nanoparticles: theory and particle size evaluation, *Anal. Chem.* 87 (2015) 7446–7453, <https://doi.org/10.1021/acs.analchem.5b01690>.
- [13] R.D. Martin, P.R. Unwin, Theory and experiment for the substrate generation tip collection mode of the scanning electrochemical microscope: application as an approach for measuring the diffusion coefficient ratio of a redox couple, *Anal. Chem.* 70 (1998) 276–284, <https://doi.org/10.1021/ac970681p>.
- [14] L. Ferna, D.A. Walsh, A.J. Bard, Thermodynamic guidelines for the design of bi-metallic catalysts for oxygen electroreduction and rapid screening by scanning electrochemical microscopy. M - Co (M : Pd, Ag, Au), *J. Am. Chem. Soc.* 127 (2005) 357–365.
- [15] D.A. Walsh, J.L. Fernández, A.J. Bard, Rapid screening of bimetallic electrocatalysts for oxygen reduction in acidic media by scanning electrochemical microscopy, *J. Electrochem. Soc.* 153 (2006) E99–E103, <https://doi.org/10.1149/1.2186208>.
- [16] J. Kim, C. Renault, N. Nioradze, N. Arroyo-Curras, K.C. Leonard, A.J. Bard, Electrocatalytic activity of individual Pt nanoparticles studied by nanoscale scanning electrochemical microscopy, *J. Am. Chem. Soc.* 138 (2016) 8560–8568, <https://doi.org/10.1021/jacs.6b03980>.
- [17] M.A. O'Connell, A.J. Wain, Mapping electroactivity at individual catalytic nanostructures using high-resolution scanning electrochemical-scanning ion conductance microscopy, *Anal. Chem.* 86 (2014) 12100–12107, <https://doi.org/10.1021/ac502946q>.
- [18] I. Turyan, M. Etienne, D. Mandler, W. Schuhmann, Improved resolution of local metal deposition by means of constant distance mode scanning electrochemical microscopy, *Electroanalysis* 17 (2005) 538–542, <https://doi.org/10.1002/elan.200403179>.
- [19] S. Jayaraman, A.C. Hillier, Screening the reactivity of Pt<sub>x</sub> Ru<sub>y</sub> and Pt<sub>x</sub> Ru<sub>y</sub> Mo<sub>z</sub> catalysts toward the hydrogen oxidation reaction with the scanning electrochemical microscope, *J. Phys. Chem. B* 107 (2003) 5221–5230, <https://doi.org/10.1021/jp0274886>.
- [20] C.M. Sánchez-Sánchez, A.J. Bard, Hydrogen peroxide production in the oxygen reduction reaction at different electrocatalysts as quantified by scanning electrochemical microscopy, *Anal. Chem.* 81 (2009) 8094–8100, <https://doi.org/10.1021/Ac901291v>.
- [21] A. Kishi, M. Inoue, M. Umeda, Scanning electrochemical microscopy study of H<sub>2</sub>O<sub>2</sub> byproduct during O<sub>2</sub> reduction at Pt/C-Nafion composite cathode, *J. Phys. Chem. C* 114 (2010) 1110–1116, <https://doi.org/10.1021/jp99010q>.
- [22] M.A. O'Connell, J.R. Lewis, A.J. Wain, Electrochemical imaging of hydrogen peroxide generation at individual gold nanoparticles, *Chem. Commun.* 51 (2015) 10314–10317, <https://doi.org/10.1039/C5CC01640A>.
- [23] J.V. Macpherson, P.R. Unwin, Combined scanning electrochemical-atomic force microscopy, *Anal. Chem.* 72 (2000) 276–285, <https://doi.org/10.1021/ac990921w>.
- [24] M.R. Nellist, Y. Chen, A. Mark, S. Gödrich, C. Stelling, J. Jiang, R. Poddar, C. Li, R. Kumar, G. Papastavrou, M. Retsch, B.S. Brunschwig, Z. Huang, C. Xiang, S.W. Boettcher, Atomic force microscopy with nanoelectrode tips for high resolution electrochemical, nano-adhesion and nanoelectrical imaging, *Nanotechnology* 28 (2017) 095711–095729, <https://doi.org/10.1088/1361-6528/aa5839>.
- [25] J. Clausmeyer, P. Wilde, T. Löffler, E. Ventosa, K. Tschulik, W. Schuhmann, Detection of individual nanoparticle impacts using etched carbon nanoelectrodes, *Electrochem. Commun.* 73 (2016) 67–70, <https://doi.org/10.1016/j.elecom.2016.11.003>.
- [26] S.C.S. Lai, P.V. Dudin, J.V. MacPherson, P.R. Unwin, Visualizing zeptomole (electro)catalysis at single nanoparticles within an ensemble, *J. Am. Chem. Soc.* 133 (2011) 10744–10747, <https://doi.org/10.1021/ja203955b>.
- [27] S. Kolagatla, P. Subramanian, A. Schechter, Nanoscale mapping of catalytic hot-spots on Fe, N-modified HOPG by scanning electrochemical microscopy-atomic force microscopy, *Nanoscale* 10 (2018) 6962–6970, <https://doi.org/10.1039/C8NR00849C>.
- [28] A. Anne, A. Chovin, C. Demaille, M. Lafouresse, High-resolution mapping of redox-immunomarked proteins using electrochemical-atomic force microscopy in molecule touching mode, *Anal. Chem.* 83 (2011) 7924–7932, <https://doi.org/10.1021/ac201907v>.
- [29] K. Huang, A. Anne, M.A. Bahri, C. Demaille, Probing individual redox PEGylated gold nanoparticles by electrochemical-atomic force microscopy, *ACS Nano* 7 (2013) 4151–4163, <https://doi.org/10.1021/nn400527u>.
- [30] A. Ghorbal, F. Grisotto, J. Charlier, S. Palacin, C. Goyer, C. Demaille, A. Braham, Nano-electrochemistry and nano-electrografting with an original combined AFM-SECM, *Nanomaterials* 3 (2013) 303–316, <https://doi.org/10.3390/nano3020303>.
- [31] H. Sugimura, N. Shimo, N. Kitamura, H. Masuhara, K. Itaya, Topographical imaging of Prussian Blue surfaces by direct-mode scanning electrochemical microscopy, *J. Electroanal. Chem.* 346 (1993) 147–160, [https://doi.org/10.1016/0022-0728\(93\)85009-6](https://doi.org/10.1016/0022-0728(93)85009-6).
- [32] R.C. Tenent, D.O. Wipf, Patterning and imaging of oxides on glassy carbon electrode surfaces by scanning electrochemical microscopy, *J. Electrochem. Soc.* 150 (2003) E131–E139, <https://doi.org/10.1149/1.1538227>.
- [33] S. González, J.J. Santana, Y. González-García, L. Fernández-Mérida, R.M. Souto, Scanning electrochemical microscopy for the investigation of localized degradation processes in coated metals: effect of oxygen, *Corros. Sci.* 53 (2011) 1910–1915, <https://doi.org/10.1016/j.corsci.2011.02.008>.
- [34] S. Kolagatla, P. Subramanian, A. Schechter, Insights on the electrochemical atomic force microscopic catalytic oxygen reduction on tip guided platinum particle deposits, *Electrochim. Acta* 217 (2016) 100–107, <https://doi.org/10.1016/j.electacta.2016.09.042>.
- [35] J.-M.M. Noël, A. Latus, C. Lagrost, E. Volanschi, P. Hapiot, Evidence for OH radical production during electrocatalysis of oxygen reduction on Pt surfaces: consequences and application, *J. Am. Chem. Soc.* 134 (2012) 2835–2841, <https://doi.org/10.1021/ja211663t>.
- [36] K.A. Kurak, A.B. Anderson, Nitrogen-treated graphite and oxygen electroreduction on pyridinic edge sites, *J. Phys. Chem. C* 113 (2009) 6730–6734, <https://doi.org/10.1021/jp811518e>.
- [37] F.-R.F. Fan, A.J. Bard, Electrochemical detection of single molecules, *Science* 267 (1995) 871–874 <http://science.sciencemag.org/content/267/5199/871>.
- [38] T. Lopes, V.A. Paganin, E.R. Gonzalez, The effects of hydrogen sulfide on the polymer electrolyte membrane fuel cell anode catalyst: H<sub>2</sub>S-Pt/C interaction products, *J. Power Sources* 196 (2011) 6256–6263, <https://doi.org/10.1016/j.jpowsour.2011.04.017>.